

A near-global climatology of oceanic coherent eddies

Josué Martínez-Moreno¹, Andrew McC. Hogg¹, and Matthew H. England²

¹Research School of Earth Science and ARC Center of Excellence for Climate Extremes, Australian National University, Canberra, Australia

²Climate Change Research Centre (CCRC), UNSW Australia, Sydney NSW, Australia

Key Points:

- Coherent eddies contain around 50% of the total surface ocean kinetic energy budget.
- Seasonal cycle of the number of coherent eddies and the coherent eddy amplitude reveals a 3-6 month lag to wind forcing.
- The seasonal lag between the number and the amplitude of coherent eddies suggests a role for the inverse cascade.

13 **Abstract**

14 Ocean eddies influence regional and global climate through mixing and transport of heat
15 and properties. One of the most recognizable and ubiquitous features of oceanic eddies
16 are coherent vortices with spatial scales of tens to hundreds of kilometers, frequently re-
17 ferred as “mesoscale eddies”. Coherent mesoscale eddies are known to transport prop-
18 erties across the ocean and to locally affect near-surface wind, cloud properties, and rain-
19 fall patterns. Although coherent eddies are ubiquitous, their climatology, seasonality, and
20 long-term temporal evolution remains poorly understood. Here, we examine the kinetic
21 energy contained in coherent eddies and present the seasonal, interannual and long-term
22 variability using satellite observations between 1993 and 2019. A total of \sim 37 million
23 coherent eddies are detected in this analysis. Around 50% of the kinetic energy contained
24 by ocean eddies corresponds to coherent eddies. Additionally, a strong seasonal cycle is
25 observed, with a 3–6 month lag between the wind forcing and the response of the coher-
26 ent eddy field. The seasonality of the number of coherent eddies and their amplitude re-
27 veals that the number of coherent eddies responds faster to the forcing (\sim 3 months), than
28 the coherent eddy amplitude (which lags by \sim 6 months). This seasonal cycle is spatially
29 variable, so we also analyze the eddy climatology in key oceanic regions. Our analysis
30 highlights the relative importance of the coherent eddy field in the ocean kinetic energy
31 budget, implies a strong response of the eddy number and eddy amplitude to forcing at
32 different time-scales, and showcases the seasonality, and multidecadal trends of coher-
33 ent eddy properties.

34 **Plain language summary**

35 Coherent eddies are the most common feature of ocean variability observable from
36 satellites. They are crucial in ocean dynamics as they can transport properties over long
37 distances and interact with the atmosphere. Our study investigates the seasonal, inter-
38 annual, and long-term changes in the abundance and intensity of coherent eddies, by au-
39 tomatically identifying individual eddies over the available satellite altimeter record. The
40 seasonal cycle suggests a transition from numerous, smaller, and weaker coherent eddies,
41 to fewer and larger, and stronger coherent eddies over the season. In addition, a long-
42 term adjustment of the coherent eddy field is identified with possible links to long-term
43 changes in the climate system.

44 1 Introduction

45 Mesoscale ocean variability with spatial scales of tens to hundreds of kilometers is
 46 comprised of processes such as vortices, waves, and jets (Ferrari & Wunsch, 2009; Fu et
 47 al., 2010). These mesoscale processes are highly energetic, and they play a crucial role
 48 in the transport of heat, salt, momentum, and other tracers through the ocean (Gill et
 49 al., 1974; Wyrtki et al., 1976; Wunsch & Ferrari, 2004). One of the most recognizable
 50 and abundant ocean processes observable from space are mesoscale vortices. Although
 51 mesoscale vortices are commonly referred to in the literature as “mesoscale eddies”, this
 52 term is also often used to describe the total mesoscale ocean variability (the time-varying
 53 component of the mesoscale flow). Thus, to avoid ambiguity we will refer to mesoscale
 54 vortices as *coherent eddies*. Coherent eddies are abundant and energetic; they are essen-
 55 tial to ocean dynamics as concluded by many previous studies (Hogg & Blundell, 2006;
 56 Siegel et al., 2011; Beron-Vera et al., 2013; Frenger et al., 2013, 2015; Pilo et al., 2015;
 57 Schubert et al., 2019; Patel et al., 2020).

58 Coherent eddies are quasi-circular geostrophic currents. According to their rota-
 59 tional direction and the sign of the Coriolis parameter, the sea surface height anomaly
 60 within a coherent eddy can be negative or positive (cold-core and warm-core coherent
 61 eddies, respectively). This characteristic sea surface height signature of coherent eddies
 62 has been utilized to identify and track coherent eddies from satellite altimetry (e.g., Chel-
 63 ton et al., 2007; Faghmous et al., 2015; Ashkezari et al., 2016; Martínez-Moreno et al.,
 64 2019; Cui et al., 2020). Automated algorithms for identification of coherent eddies have
 65 revealed their ubiquity in the oceans, with a predominant influence at hotspots of eddy
 66 activity such as in boundary current extensions and the Antarctic Circumpolar Current.
 67 In these regions, it has been estimated that coherent eddies contribute around 40–50%
 68 of the net mesoscale kinetic energy (Chelton et al., 2011) and thus a significant fraction
 69 of the total kinetic energy (Ferrari & Wunsch, 2009). Although this estimate showcases
 70 the importance of the mesoscale coherent eddy field, the energy contained in coherent
 71 eddies was estimated by extracting the total geostrophic velocity within the radius of
 72 each detected coherent eddy; thus, it is possible that this estimate may contain energy
 73 from other processes. Here we extend on this past work by reconstructing the surface
 74 imprint of coherent eddies using a new eddy tracking algorithm and using the latest avail-
 75 able satellite record.

76 There is broad consensus that mesoscale eddy kinetic energy has a pronounced sea-
77 sonal variability (Qiu, 1999; Qiu & Chen, 2004; Kang & Curchitser, 2017; Uchida et al.,
78 2017). Several hypotheses have been proposed to explain this seasonality including: sea-
79 sonal variations of atmospheric forcing (Sasaki et al., 2014), seasonality of the mixed layer
80 depth (Qiu et al., 2014; Callies et al., 2015), seasonality of the intensity of barotropic in-
81 stability (Qiu & Chen, 2004), the variability of the baroclinic instability due to the sea-
82 sonality of the vertical shear (Qiu, 1999), and a seasonal lag of the inverse energy cas-
83 cade (i.e. energy is transported between scales, from small to large; Arbic et al., 2013)
84 in combination with the presence of a front in the mixed layer, which can lead to a sea-
85 sonal cycle of the baroclinic instability (Qiu et al., 2014). On one hand, processes such
86 as barotropic and baroclinic instabilities control the seasonality of coherent eddies in the
87 ocean. On the other hand, recent studies using observations and eddy-permitting climate
88 models suggest slower adjustments of the global ocean that create long-term changes in
89 the coherent eddy field. Such readjustments include a multidecadal increase in the ocean
90 stratification resulting from temperature and salinity changes (Li et al., 2020), a hori-
91 zontal readjustment of sea surface temperature gradients (Cane et al., 1997; Bouali et
92 al., 2017; Ruela et al., 2020), and an intensification of the kinetic energy, eddy kinetic
93 energy, and mesoscale eddy kinetic energy over the last 3 decades as a consequence of
94 an increase in wind forcing (Hu et al., 2020; Wunsch, 2020; Martínez-Moreno et al., 2021).
95 All of these seasonal factors and long-term readjustments directly influence the annual
96 and decadal response of the coherent eddy field, however, the seasonality of the coher-
97 ent component of the eddy kinetic energy, as well as the seasonal cycle and trends of the
98 coherent eddy statistics, remain unknown.

99 Here we present a new global climatology of the coherent eddy kinetic energy by
100 reconstructing the coherent eddy signature from satellite observations. Our study doc-
101 uments the seasonal cycle of the coherent eddy kinetic energy, and the seasonal cycle and
102 long-term trends of the coherent eddy properties over the satellite record. Moreover, we
103 conduct more detailed analyses in regions where coherent eddies dominate the eddy ki-
104 netic energy field. The rest of this paper is structured as follows: the data sources and
105 methodology are described in Section 2. Then, we present the climatology, energy ra-
106 tios, and global seasonality of the coherent eddy kinetic energy in Section 3. Section 4
107 outlines the global climatology and seasonality of coherent eddy properties, followed by
108 long-term changes of the coherent eddy properties (Section 5). Then we focus our at-

109 tention on the seasonal cycle and coherent eddy properties in regions dominated by co-
110 herent eddies (Section 6). Finally, Section 7 summarizes the main results and discusses
111 the implications of this study.

112 **2 Methods**

113 We use daily sea surface height (SSH) data made available by the Copernicus Ma-
114 rine Environment Monitoring Service in near real time (CMEMS, 2017). This gridded
115 product contains the sea surface height and geostrophic velocities with daily 0.25° res-
116 olution from January 1993 to December 2019. The daily geostrophic velocities allow us
117 to compute the kinetic energy (KE) and eddy kinetic energy (EKE) over the satellite record.
118 The main source of EKE is the time-varying wind (Ferrari & Wunsch, 2009); thus, we
119 also compute the seasonal cycle of the wind magnitude from the JRA55 reanalysis (Japan
120 Meteorological Agency, Japan, 2013) using wind velocities at 10m above the ocean's sur-
121 face.

122 Over the same record, coherent eddy statistics from Martínez-Moreno et al. (2019),
123 hereafter MM19, are analyzed and compared with those released by Chelton & Schlax
124 (2013), hereafter CS13. Both datasets are gridded at 1° resolution and are produced via
125 automated eddy identification algorithms using closed contours of SSH. However, these
126 datasets have important differences in the criteria they use to identify and record coher-
127 ent eddy statistics. The major differences include: (i) MM19's algorithm requires an ad-
128 justment between a 2D Gaussian and the SSH anomaly (SSHa) surface within the iden-
129 tified closed contour, while CS13's only uses the outermost closed contour of SSH; (ii)
130 MM19's dataset reports the maximum SSHa within the identified coherent eddy, while
131 CS13's algorithm reports the maximum SSH value minus the discrete level in which the
132 coherent eddy was identified; and (iii) MM19's dataset includes all detected coherent ed-
133 dies, while CS13's dataset excludes coherent eddies with lifetimes shorter than four weeks
134 and coherent eddy amplitudes smaller than 1cm. Moreover, MM19's algorithm allows
135 the reconstruction of the coherent eddy field under the assumption that coherent eddies
136 have a 2D Gaussian imprint in the sea surface height. This Gaussian reconstruction of
137 the coherent eddy field then allows us to estimate the coherent geostrophic eddy veloc-
138 ities and thus the kinetic energy contained only in coherent eddies.

139 **2.1 Kinetic Energy decomposition**

140 Kinetic energy is commonly divided into the mean and time-varying components
 141 through a Reynolds decomposition. At a given time, the surface velocity field $\mathbf{u} = (u, v)$
 142 is split into the time mean ($\bar{\mathbf{u}}$) and time varying components (\mathbf{u}'). Moreover, MM19 pro-
 143 posed to further decompose the eddy kinetic energy into the energy of coherent features
 144 (\mathbf{u}'_e) and non-coherent features (\mathbf{u}'_n). Therefore the KE equation can be written as:

$$\text{KE} = \underbrace{\bar{u}^2 + \bar{v}^2}_{\text{MKE}} + \underbrace{u'_e^2 + v'_e^2}_{\text{CEKE}} + \underbrace{u'_n^2 + v'_n^2}_{\text{nCEKE}} + \mathcal{O}_c^2 + \mathcal{O}^2 \quad (1)$$

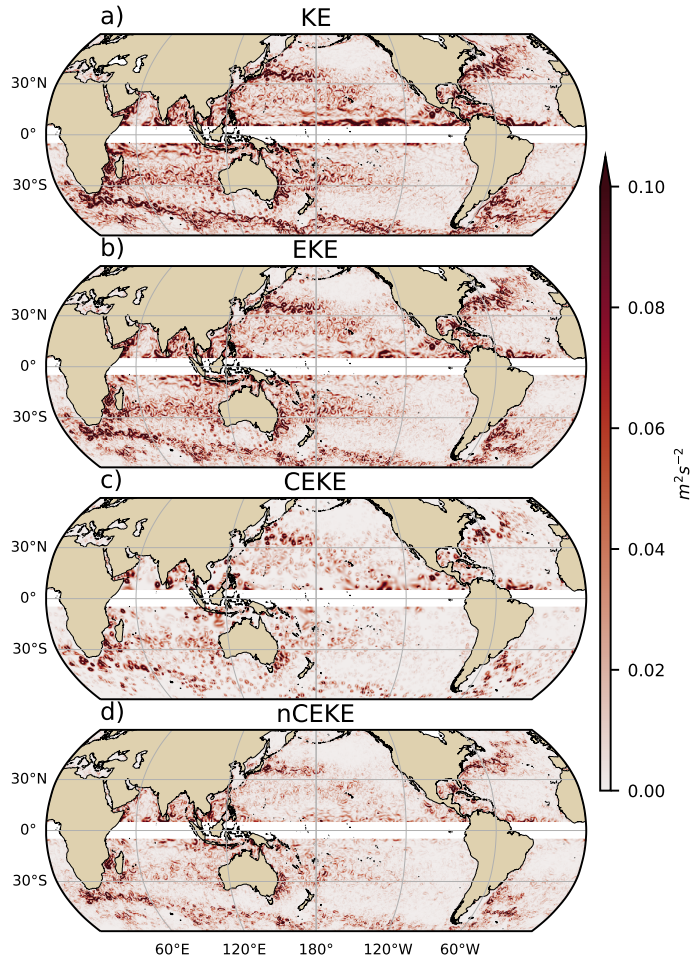
145 Due to the properties of this decomposition, the term \mathcal{O}^2 is zero when averaged
 146 over the same period as $\bar{\mathbf{u}}$. However, \mathcal{O}_c^2 is not necessarily negligible, unless it is aver-
 147 aged over time and space. More information about the decomposition of the field into
 148 coherent features and non-coherent features is explained in Martínez-Moreno et al. (2019).
 149 A global snapshot of each component of kinetic energy decomposition is shown in Fig-
 150 ure 1, where the KE and EKE are comprised of rings and filaments. As expected, the
 151 decomposition of EKE into CEKE and nCEKE components exhibits only the ring-like
 152 signatures expected of coherent eddies, while the non-coherent component primarily shows
 153 filaments, with some mis-identified coherent eddies.

157 **2.2 Eddy statistics**

158 The eddy statistics used in this study include (i) the eddy count ($cEddy_n$) defined
 159 as the number of coherent eddies per grid cell, (ii) the eddy diameter defined as the di-
 160 ameter of a circle with equal area to the closed contour of each identified eddy, and (iii)
 161 the mean eddy amplitude defined as the mean amplitude of the coherent eddies within
 162 the cell ($cEddy_{amp}$). The latter metric can be separated into positive ($cEddy_{amp}^+$) and
 163 negative ($cEddy_{amp}^-$) coherent eddy amplitudes, defined as the mean amplitude of warm
 164 core and cold core coherent eddies, respectively, within the cell. The polarity indepen-
 165 dent eddy amplitude ($|cEddy_{amp}|$) is defined as:

$$|cEddy_{amp}| = \frac{1}{2} (cEddy_{amp}^+ - cEddy_{amp}^-) \quad (2)$$

166 Note that the $cEddy_{amp}^+$ and $cEddy_{amp}^-$ are sign definite, thus the difference will always
 167 be positive, whereas the gridded averaged $cEddy_{amp}$ can be negative or positive noting



154 **Figure 1.** Snapshot of surface kinetic energy (KE), surface eddy kinetic energy (EKE),
 155 surface coherent eddy kinetic energy (CEKE), and surface non-coherent eddy kinetic energy
 156 (nCEKE) for the 1st of January 2017.

168 the dominant polarity of coherent eddies in the region, and the absolute value of $cEddy_{amp}$
 169 is denoted by $cEddy_{|amp|}$. We analyze the climatology and trends of the above eddy statis-
 170 tics over the available satellite record, namely between 1993 and 2019. We exclude the
 171 equatorial region (10°S - 10°N) and regions poleward of 60° , because the geostrophic ap-
 172 proximation is invalid near the Equator and the satellite spatial coverage at high-latitudes
 173 is unable to resolve the coherent eddy scales polewards of 60° . Note that the climatol-
 174 ogy of $cEddy_n$ is computed by adding all the identified eddies over the record, while all
 175 other climatological statistics are computed as the time-average over the record. Sea-
 176 sonal climatologies are calculated for the monthly average of each coherent eddy statis-

tic, while hemispheric time-series are filtered with a running average of 90 days. Trends of $cEddy_n$ and $|cEddy_{amp}|$ are calculated by coarsening the dataset to a 5° grid, and then linear trends are computed for each grid point. The statistical significance of trends is assessed by a modified Mann-Kendall test above the 95% confidence level (Yue & Wang, 2004).

Time averages are denoted by $\overline{}$, while area-weighted averages are denoted using $\langle \rangle$, where the area-weighted average of a function f is:

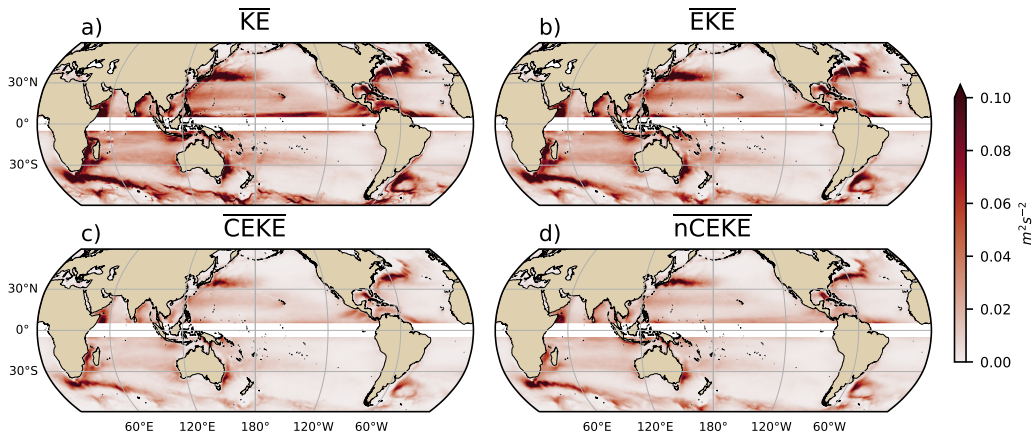
$$\langle f \rangle = \frac{\int f \xi dx dy}{\int \xi dx dy}, \quad (3)$$

where ξ is a mask that is set to zero in grid cells where no coherent eddies were identified and one elsewhere.

3 Global Coherent Eddy Energetics

The kinetic energy decomposition estimated from sea surface height measured by satellite altimeters averaged from 1993-2019 is shown in Figure 2. These maps show that many regions of the global ocean are highly energetic in mean KE (\overline{KE}), mean EKE (\overline{EKE}), mean coherent eddy kinetic energy (\overline{CEKE}) and mean non-coherent eddy kinetic energy (\overline{nCEKE}). The spatial pattern highlights well-known regions of the ocean where mesoscale processes are abundant, such as the western boundary current (WBC) extensions and the Antarctic Circumpolar Current. The spatial distribution of the energy contained by the reconstructed mesoscale coherent eddies and non-coherent components are similar (Figures 2c,d). However, there are some regions where coherent eddies dominate over non-coherent, and vice-versa. Overall, this decomposition suggests that boundary current extensions and other energetic regions of the ocean contain both coherent and non-coherent components of the kinetic energy.

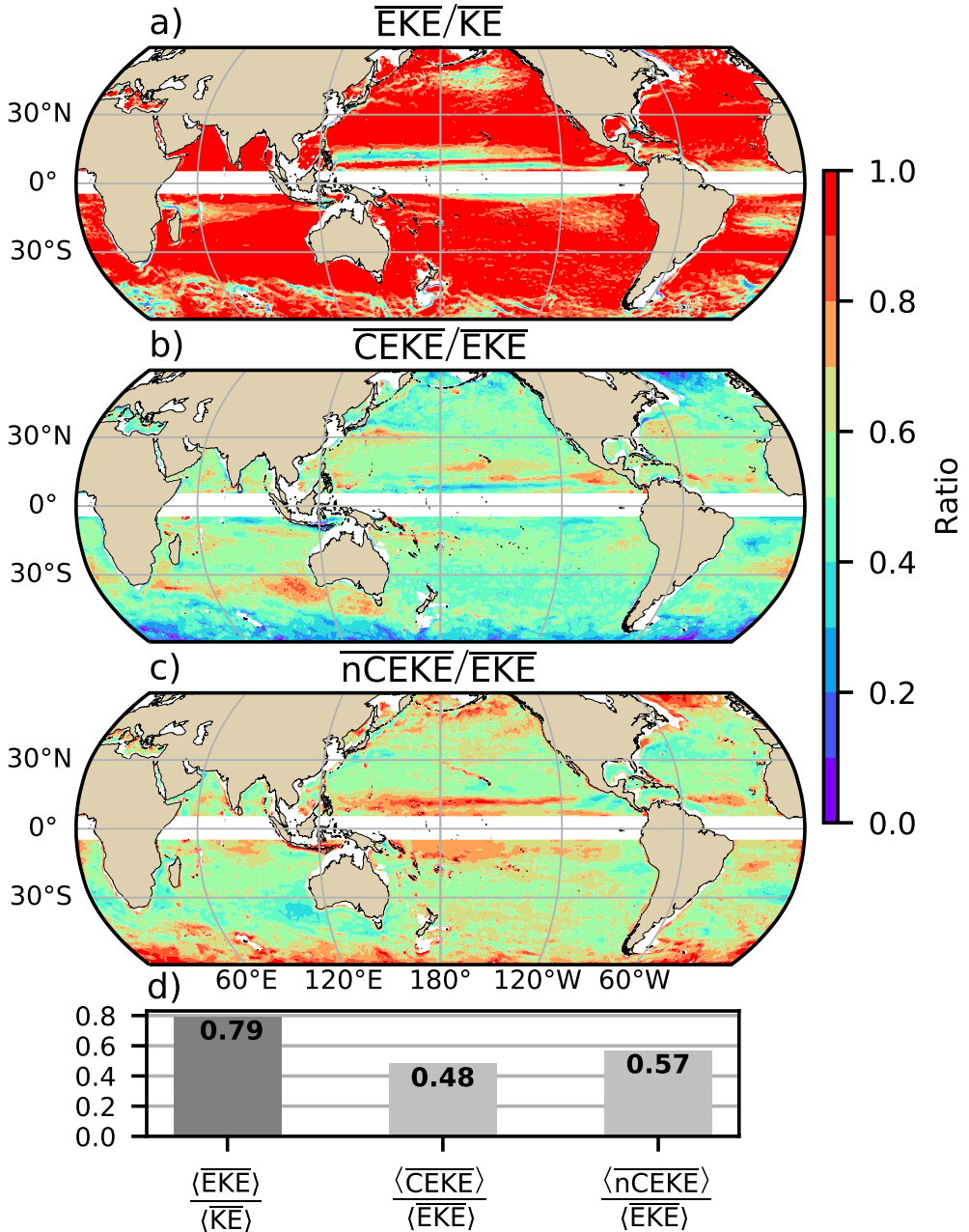
Eddy kinetic energy is known to be more than an order of magnitude greater than kinetic energy of the mean flow (MKE; Gill et al., 1974); this result is clearly shown in Figure 3a, which indicates that \overline{EKE} is responsible for almost all the \overline{KE} across the ocean, except for regions with persistent currents over time. Such regions are located in the mean boundary extension locations, the equatorial Pacific currents and regions in the Antarctic Circumpolar Current, where the \overline{EKE} explains around 40% of the \overline{KE} . In a previous study, Chelton et al. (2011) estimated that coherent eddies with lifetimes greater than 4 weeks contain between 40-60% of the \overline{EKE} . Our method to reconstruct the coherent



199 **Figure 2.** a) Mean surface kinetic energy (\overline{KE}); b) surface eddy kinetic energy (\overline{EKE}); c)
200 surface coherent eddy kinetic energy (\overline{CEKE}), and d) surface non-coherent eddy kinetic energy
201 (\overline{nCEKE}) averaged between 1993-2018.

219 eddy signature (Figure 3b) further corroborates that the coherent eddy component ($\langle \overline{CEKE} \rangle$)
220 has $\sim 48\%$ of the $\langle \overline{EKE} \rangle$ (Figure 3d). Furthermore, global area averages of the ratios show
221 that $\langle \overline{EKE} \rangle$ explains $\sim 78\%$ of the ocean $\langle \overline{KE} \rangle$ field, while non coherent eddy features
222 contain $\sim 57\%$ percent of the $\langle \overline{EKE} \rangle$. Note that the globally averaged coherent and non
223 coherent components do not add to 100% as the cross terms (\mathcal{O}_c^2) are non-zero. The spa-
224 tial pattern reveals a dominance of the \overline{CEKE} equatorward from the boundary current
225 extensions and in areas with large coherent eddy contributions of around 80% of the re-
226 gion's eddy kinetic energy, such as south of Australia, in the Tehuantepec Gulf, and in
227 the tropical Atlantic. An evident signal is a reduction of the energy contained by coher-
228 ent eddies at high latitudes and an increase in the energy explained by non-coherent ed-
229 dies; this signal could be a consequence of the inability of the 0.25° satellite resolution
230 (~ 13 km at 60° latitude) to resolve coherent eddies with scales smaller than ~ 10 km
231 (first baroclinic Rossby radius at 60° ; Chelton et al., 1998).

232 Figure 4 shows the seasonal cycle of the area-weighted EKE and CEKE for the North-
233 ern Hemisphere ($\langle EKE \rangle_{NH}$ and $\langle CEKE \rangle_{NH}$; $10^\circ N - 60^\circ N$) and Southern Hemisphere
234 ($\langle EKE \rangle_{SH}$ and $\langle CEKE \rangle_{SH}$; $60^\circ S - 10^\circ S$). In both hemispheres, the $\langle EKE \rangle$ and $\langle CEKE \rangle$
235 peak during summer. In the Northern Hemisphere, the largest $\langle EKE \rangle_{NH}$ and $\langle CEKE \rangle_{NH}$
236 occurs in July, ~ 6 months after the maximum winds in January (purple bar and black
237 star in Figure 4c and d). Meanwhile, the Southern Ocean $\langle EKE \rangle_{SH}$ and $\langle CEKE \rangle_{SH}$ sea-



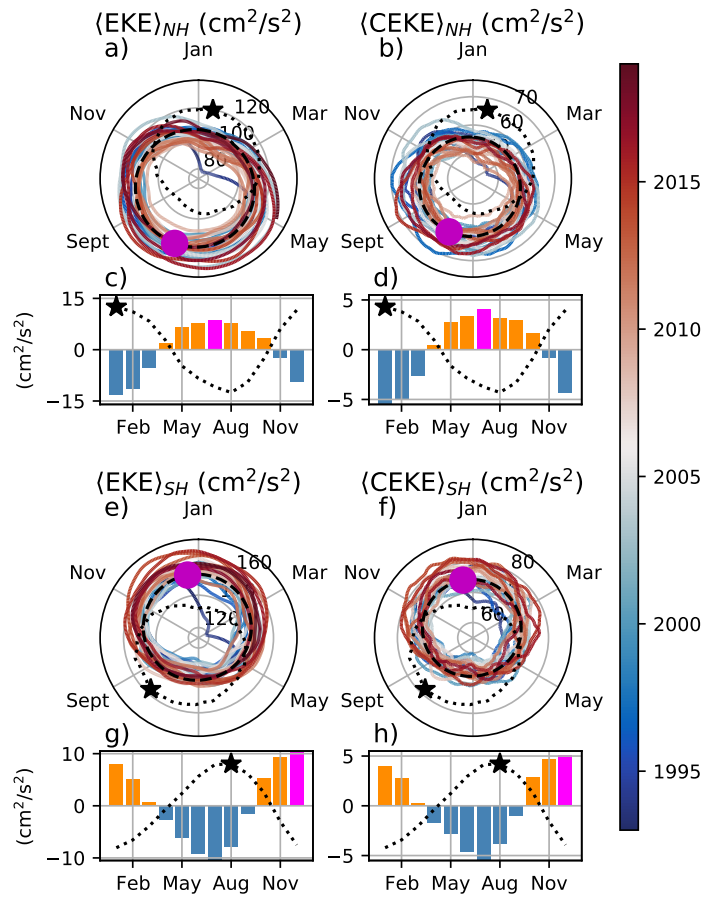
202 **Figure 3.** Ratios of the kinetic energy components. a) Map of the proportion of mean eddy
 203 kinetic energy (\overline{EKE}) versus mean kinetic energy (\overline{KE}); b) Map of the fraction of mean coherent
 204 eddy kinetic energy (\overline{CEKE}) versus mean eddy kinetic energy (\overline{EKE}); c) Map of the fraction of
 205 mean non-coherent eddy kinetic energy (\overline{nCEKE}) versus mean eddy kinetic energy (\overline{EKE}); d)
 206 Global time and area averaged (represented by $\langle \rangle$) fraction of mean eddy kinetic energy ($\langle \overline{EKE} \rangle$)
 207 versus the global mean kinetic energy ($\langle \overline{KE} \rangle$), area averaged fraction of mean coherent eddy
 208 kinetic energy ($\langle \overline{CEKE} \rangle$) and mean non coherent eddy kinetic energy ($\langle \overline{nCEKE} \rangle$) versus global
 209 mean eddy kinetic energy ($\langle \overline{EKE} \rangle$). Regions where the depth of the ocean is shallower than
 210 1000m are removed from the ratio estimation.

sonal maxima arise during December, \sim 4 months after the maximum winds in August (purple bar and back star in Figure 4g, and h). This lag between winds and the eddy and coherent eddy energy components is further discussed in Section 4.

The cyclic plots in Figure 4 show the temporal evolution of $\langle \text{EKE} \rangle$ and $\langle \text{CEKE} \rangle$. Note that high frequency variability can be observed in the $\langle \text{CEKE} \rangle$ field with temporal scales of a few months, this variability could be attributed to regional dynamics averaged over the hemisphere (boundary currents, ocean gyres, etc.), as well as errors within the coherent eddy reconstruction. Additionally, concentric changes in the cyclic plots highlight long-term changes over the record. For example, the Northern Hemisphere winters during early years of the record (blue) had a more energetic coherent eddy field, which has transitioned to weaker coherent energy content since 2010 (red), in other words, the intensity of the $\langle \text{CEKE} \rangle_{NH}$ field has decreased. A larger long-term change can be observed in the Southern Hemisphere, where concentric growth over time in $\langle \text{EKE} \rangle_{SH}$ and $\langle \text{CEKE} \rangle_{SH}$ supports the previously observed strengthening of the eddy field in the Southern Ocean (Hogg et al., 2015; Martínez-Moreno et al., 2019; Martínez-Moreno et al., 2021).

4 Global Coherent Eddy Statistics

Coherent eddy kinetic energy allows us to quantify and study the energy of the eddy field, but the coherent eddy properties computed by automated coherent eddy identification algorithms allow us to further investigate the contribution and temporal changes of their abundance (i.e. the number of eddies) and their intensity (both their amplitude and diameter). Figure 5 shows gridded estimates of the number of eddies and the eddy amplitude. In this analysis, we contrast our MM19 eddy count with that of CS13 (Chelton et al., 2007; Figure 5a-b). Although the number of identified eddies is larger in MM19, possibly due to the lifespan filter implemented by CS13, both datasets reveal consistent spatial patterns. For example, both datasets show an important meridional variation in the abundance of eddies, with high numbers of eddies in mid-latitudes and fewer eddies in the tropics and at high-latitudes (\sim 60°). Additionally, there is a tendency at mid-latitudes (30°) for higher numbers of eddies in the eastern side of ocean basins (e.g. the East North Pacific, East North Atlantic, East South Pacific, and East South Atlantic). Another interesting pattern emerges in both eddy count datasets, where small scale structures appear in the eddy count field. These small structures highlight preferred coherent eddy paths observable in boundary current extensions and over regions of the Southern Ocean.



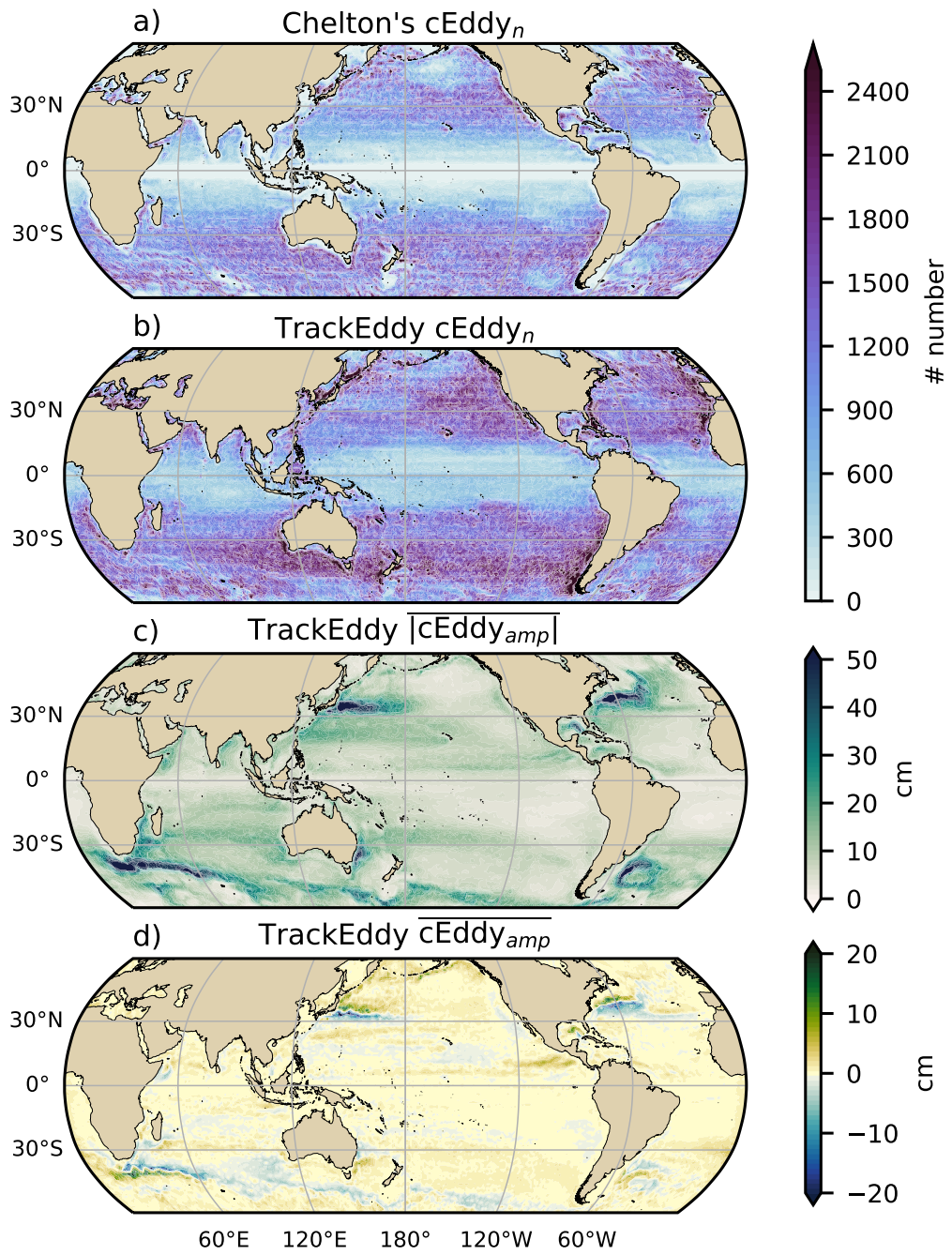
253 **Figure 4.** Seasonality of the area-weighted eddy kinetic energy ($\langle EKE \rangle$) and coherent eddy ki-
 254 netic energy ($\langle CEKE \rangle$). Panels a) and b) show the time-series of the Northern Hemisphere, while
 255 panels e) and f) correspond to the Southern Hemisphere. Panels c) and d) show the seasonal
 256 cycle of the $\langle EKE \rangle_{NH}$ and $\langle CEKE \rangle_{NH}$ in the Northern Hemisphere, and panels g) and h) show
 257 the Southern Hemisphere ($\langle EKE \rangle_{SH}$ and $\langle CEKE \rangle_{SH}$). Bars correspond to the seasonal cycle of
 258 the fields and dotted lines show the seasonal cycle of the wind magnitude smoothed over 120 days
 259 (moving average). The black stars and magenta markers (circle and bar) show the maximum of
 260 the seasonal cycle for the kinetic energy components and the wind magnitude, respectively. In
 261 the cyclic plots, line colors shows the year.

279 These structures and paths of coherent eddies could be associated with topographic fea-
 280 tures, with overall consistency between the eddy count patterns using the two different
 281 eddy identification methods.

287 Regions with large counts of eddies have, in general, small absolute amplitudes (Fig-
 288 ure 5c), for example, the eastern side of mid-latitude ocean basins. The ocean gyre in-
 289 teriors have a larger absolute amplitude and finally regions such as the boundary cur-
 290 rent extensions and the Antarctic Circumpolar Current have the largest coherent eddy
 291 absolute amplitudes, as also shown by Chelton et al. (2011). Eddy amplitude highlights
 292 regions dominated by a given coherent eddy polarity, for example, boundary current ex-
 293 tensions have a preferred sign (Figure 5 d); namely, positive amplitude polewards of the
 294 boundary current extension mean location, and negative amplitude equatorwards. This
 295 sign preference is consistent with the preferential way that coherent eddies are shed from
 296 boundary current extensions; with warm core eddies (positive) polewards of the bound-
 297 ary current extension, and equatorward for cold core eddies (negative) (Chelton et al.,
 298 2007, 2011; Kang & Curchitser, 2013). These global statistics reveal the absolute coher-
 299 ent eddy amplitude as a proxy for the CEKE with similar spatial patterns (Figure 2 &
 300 Figure 5c) and showcases that in regions where $\overline{\text{CEKE}}$ accounts for a large proportion
 301 of $\overline{\text{EKE}}$ (Figure 3), the absolute coherent eddy amplitude is also large.

302 To further understand the seasonal cycle of $\langle \text{CEKE} \rangle$, we compute the climatology
 303 of coherent eddy properties in each hemisphere (Figure 6). The seasonality of the num-
 304 ber of eddies in the Northern Hemisphere peaks in April (Figure 6a, c), while the South-
 305 ern Hemisphere maximum number of eddies occurs during October (Figure 6e, g). Mean-
 306 while, the seasonality of the eddy amplitude ($\langle |c\text{Eddy}_{amp}| \rangle$) peaks in August and Jan-
 307 uary for the Northern and Southern Hemispheres respectively (Figure 6b, d, f, and h).
 308 As expected, the seasonality of $\langle |c\text{Eddy}_{amp}| \rangle$, equivalent to the intensity of the coher-
 309 ent eddies, is consistent with the seasonal cycle of $\langle \text{CEKE} \rangle$.

310 A key feature of Figure 6 is a distinct lag of ~ 3 months between the winds and eddy
 311 count, while the eddy amplitude maximum occurs ~ 6 months after the seasonal max-
 312 imum in winds. We suggest that the eddy number increases earlier in the year and, through
 313 eddy-eddy interactions (merging of coherent eddies), the coherent eddy amplitude in-
 314 creases ~ 3 months after. This seasonal lag and summer maximum is consistent with pre-
 315 vious studies which suggest that a time-lag of the inverse cascade (Sasaki et al., 2014;

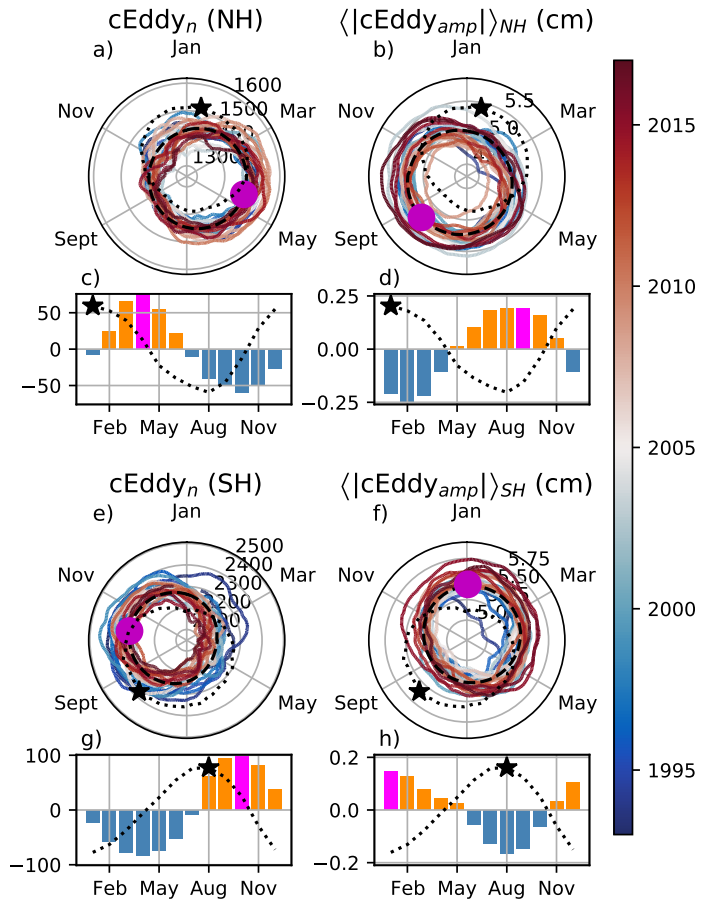


282 **Figure 5.** Averaged coherent eddy statistics. a) Climatology of the number of coherent eddies
 283 (cEddy_n) identified by Chelton et al. (2007); b) Climatology of the number of coherent eddies
 284 (cEddy_n) identified by Martínez-Moreno et al. (2019); c) Climatology of the mean absolute co-
 285 herent eddy amplitude (cEddy_{amp}), and d) Climatology of the mean coherent eddy amplitude
 286 (cEddy_{amp}).

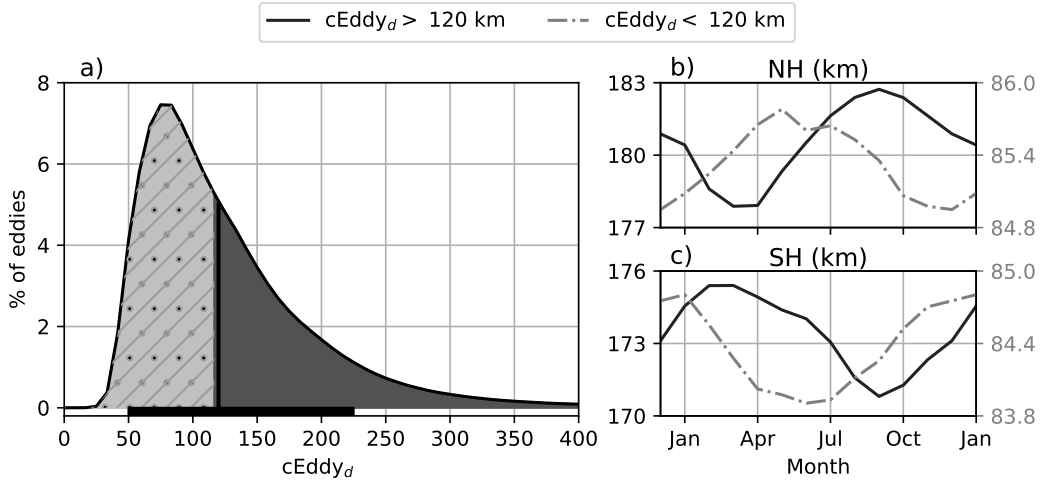
316 Qiu et al., 2014) is responsible for the EKE seasonal cycle, where winter has the high-
 317 est energy at the smallest scales (non-resolvable with satellite observations), spring and
 318 autumn have the highest and lowest energy at scales of 50-100 km, and summertime has
 319 the highest energy at the largest scales (> 100 km; Uchida et al., 2017). Thus, the max-
 320 imum of $\langle \text{EKE} \rangle$, $\langle \text{CEKE} \rangle$, and $\langle |c\text{Eddy}_{amp}| \rangle$ located during summertime suggests that
 321 the seasonality of eddies and coherent eddies could be dominated by scales larger than
 322 100 km.

323 This result can be further explored by looking at the seasonal evolution of the eddy
 324 diameter ($c\text{Eddy}_d$). Note that 90% of identified coherent eddies have diameters between
 325 50 and 220 km (Figure 7a). We partition eddies into large-scale coherent eddies (diam-
 326 eter > 120 km) and small-scale coherent eddies (diameter < 120 km; Figure 7a). In the
 327 Northern Hemisphere, small-scale eddies have a seasonal peak in diameter during May,
 328 while large-scale eddies have the greatest diameter in September (Figure 7b). Meanwhile,
 329 in the Southern Hemisphere, the small-scale coherent eddies exhibit maximum dia-
 330 meter in December, while the diameter of large-scale coherent eddies peaks in February (Fig-
 331 ure 7 c). This result suggests that wind driven baroclinic instabilities generate small co-
 332 herent eddies early in the season, which then merge and grow to become larger in diam-
 333 eter and amplitude, and thus, more energetic. This process is likely associated with the
 334 inverse energy cascade, and suggests that this mechanism not only drives EKE season-
 335 ality, but also may be responsible for the seasonal cycle of coherent eddies.

351 Long-term changes can be observed in Figure 6a,b, e, and f where growing/shrinking
 352 concentric circles over time denote an trend of the field. This trend is particularly ev-
 353 ident in the Southern Hemisphere, where the number of eddies has decreased, while the
 354 eddy amplitude has increased. This result is consistent with the observed trends in EKE
 355 and mesoscale EKE in the Southern Ocean (Hogg et al., 2015; Martínez-Moreno et al.,
 356 2019). The coherent eddy amplitude from positive coherent eddies and negative coher-
 357 ent eddies show similar seasonal cycles to the absolute eddy amplitude. The Northern
 358 Hemisphere decrease in absolute eddy amplitude is driven by a decrease of the ampli-
 359 tude of negative coherent eddies in the Northern Hemisphere. Meanwhile in the South-
 360 ern Ocean, the increase in absolute eddy amplitude is corroborated by a strengthening
 361 of both coherent eddy polarities since the early 90s.



336 **Figure 6.** Seasonality of the count of number of eddies ($c\text{Eddy}_n$) and the area-weighted polar-
 337 ity independent coherent eddy amplitude ($\langle |c\text{Eddy}_{amp}| \rangle$); Panels a and b show the time-series of
 338 the Northern Hemisphere, while panels e and f correspond to the Southern Hemisphere. Panels c
 339 and d show the seasonal cycle of $c\text{Eddy}_n$ and $\langle |c\text{Eddy}|_{amp} \rangle_{NH}$ in the Northern Hemisphere, and
 340 panels g and h show the Southern Hemisphere, $c\text{Eddy}_n$ and $\langle |c\text{Eddy}|_{amp} \rangle_{SH}$. Bars correspond to
 341 the seasonal cycle of the fields and dotted lines show the seasonal cycle of the wind magnitude,
 342 smoothed over 120 days (moving average). The black stars and magenta markers (circle and
 343 bar) indicate the maximum of the seasonal cycle for the eddy property, and the wind magnitude,
 344 respectively. In the cyclic plots, line color show the year from 1993-2019.

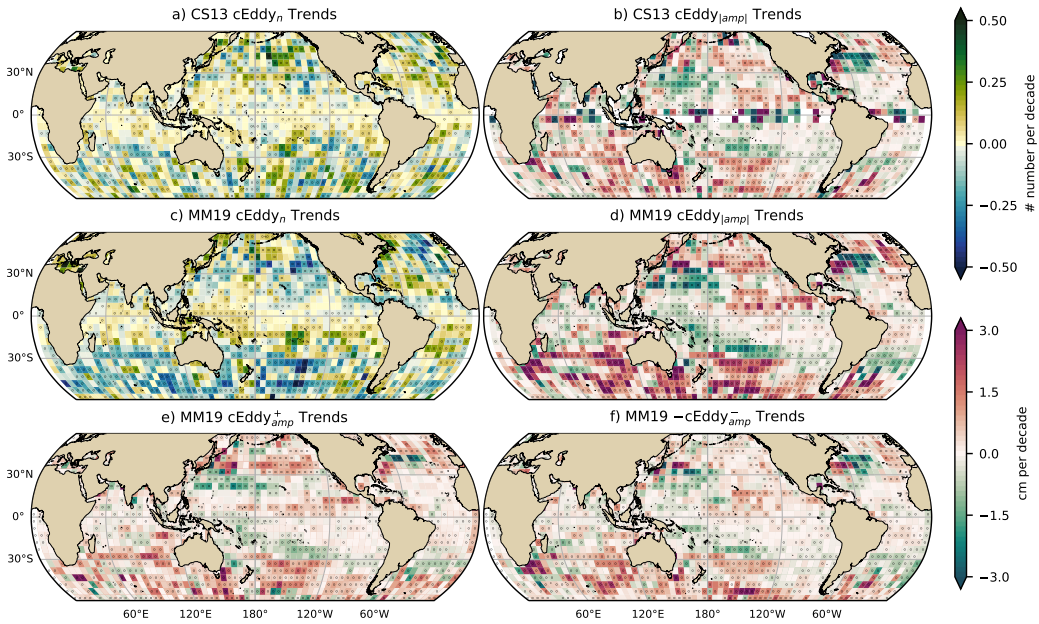


345 **Figure 7.** Distribution of the identified eddy diameter ($cEddy_d$; km) and hemispherical
 346 seasonality of the coherent eddy diameter. a) Distribution in percentage of identified eddy am-
 347 plitude, solid bar below distribution represents 90% of the identified eddies. Seasonal cycle of
 348 the eddy diameter for the b) Northern Hemisphere and c) Southern Hemisphere. Dark solid line
 349 and area corresponds to coherent eddies with diameters larger than 120 km, while light gray
 350 eddies with diameters smaller than 120 km.

362 5 Trends

363 The results presented in Figures 4 and 6 suggest a long-term readjustment of the
 364 coherent eddy field. The long-term trends of the number of coherent eddies, absolute co-
 365 herent eddy amplitude, and coherent eddy amplitude polarities are further explored in
 366 Figure 8 contrasting the MM19 and CS13 methods. Both MM19 and CS13 datasets show
 367 consistent spatial patterns in the trends and significance of the number of coherent ed-
 368 dies and the absolute coherent eddy amplitude. Several regions in the ocean, such as the
 369 Southern Ocean, North Atlantic and North Pacific, show a decrease in the number of ed-
 370 dies. Those same regions also have a clear increase in the absolute coherent eddy am-
 371 plitude. These trends are similar to those observed in mesoscale eddy kinetic energy (Martínez-
 372 Moreno et al., 2021) and provide additional evidence of a readjustment of the mesoscale
 373 eddy field over the last 3 decades.

374 The observed trends of $cEddy_{amp}$ in several oceanic regions have the same scale
 375 as sea level rise (~ 3 cm per decade). By analyzing the positive and negative coherent eddy
 376 amplitude, we filter out the observed trends that come from a net increase in sea level.



384 **Figure 8.** Trends of coherent eddy statistics. a) and c) Trends of the number of identified
 385 coherent eddies from satellite observations identified reported in CS13's dataset and using the
 386 TrackEddy scheme of MM19. b) and d) Trends of the absolute value of identified coherent eddy
 387 amplitude ($cEddy_{amp}$) from satellite observations reported by CS13 and TrackEddy (after
 388 MM19). e) and f) Trends of the eddy amplitude polarity using TrackEddy ($cEddy_{amp}^+$ and
 389 $cEddy_{amp}^-$). Gray stippling shows regions that are statistically significant above the 95% con-
 390 fidence level.

377 In fact, each coherent eddy polarity has intensified in the Southern Ocean and North East
 378 Pacific and Atlantic. In other words, the amplitude of each polarity has increased over
 379 time, and thus this strengthening is an intrinsic response of the coherent eddy field. Note
 380 that the negative coherent eddy amplitude dominates the global $|cEddy_{amp}|$ trends (Fig-
 381 ure 8e, f). However, different trend patterns can be observed in both positive and neg-
 382 ative coherent eddy amplitudes in the North Atlantic and North Pacific, where the neg-
 383 ative coherent eddy amplitude in the Western Boundary Currents appears to decrease.

391 6 Regional Climatology

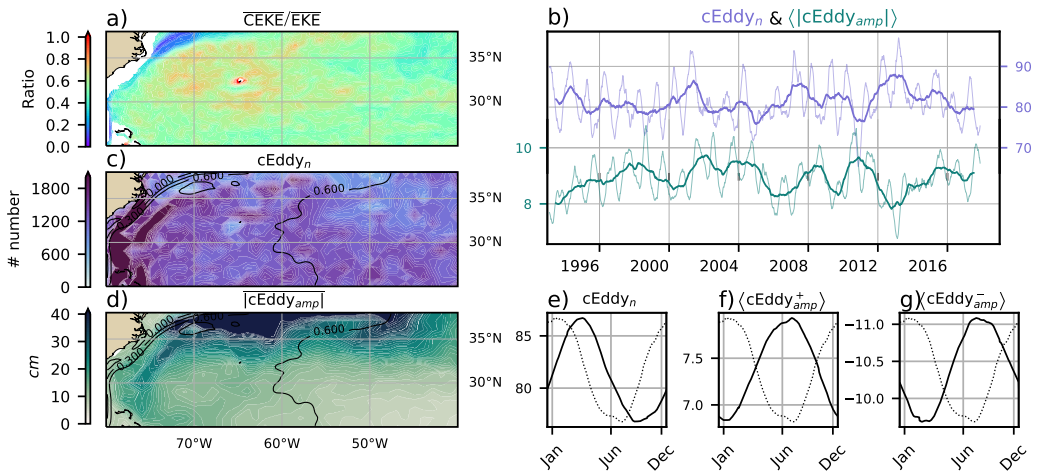
392 For regions with relatively large proportions of CEKE located at WBC extensions
 393 and eastern boundary currents, we investigate the seasonal and long-term variability of
 394 the coherent eddy properties. The most energetic WBCs include the Gulf Stream, the

395 Kuroshio Current, and the Agulhas Current (Figures 9, 10, and 11). Coherent eddy gen-
 396 eration in boundary current extensions occurs through baroclinic and barotropic insta-
 397 bilities of the mean current, thus all these regions share similar generation dynamics. In
 398 all these regions without exception; (i) CEKE contains 50-80% of the EKE in regions
 399 equatorward from the mean WBC extensions, (ii) the number of eddies is consistently
 400 small over the mean WBC extensions, and (iii) the eddy amplitude is larger over the mean
 401 WBC extensions.

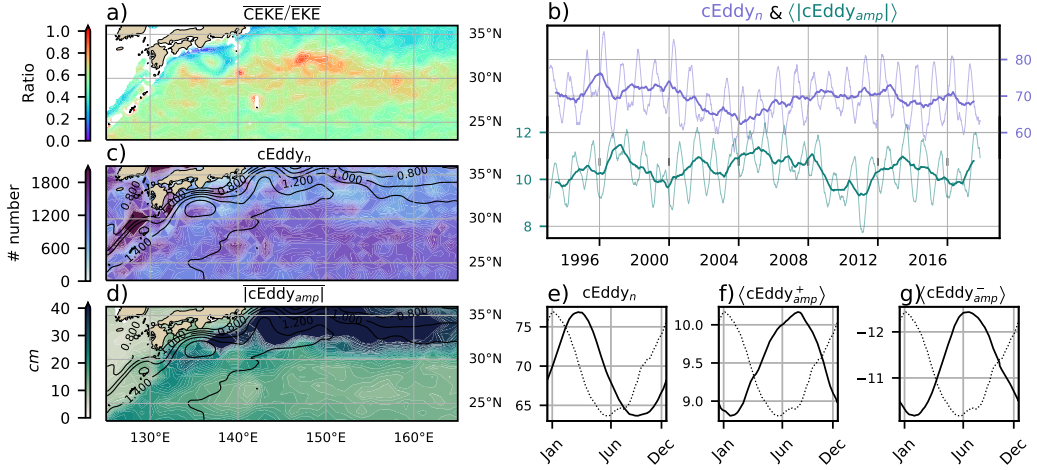
402 In the Gulf Stream, the energy ratio between CEKE and EKE is \sim 56% (Figure 9).
 403 The highest energy ratio occurs in regions with numerous eddies, colocated with regions
 404 where the largest $|cEddy_{amp}|$ gradients occur. The time series of $cEddy_n$ and $\langle |cEddy_{amp}| \rangle$
 405 are anti-correlated (-0.52), and they display interannual and seasonal variability. Although
 406 Chaudhuri et al. (2009) observed that a positive phase of the North Atlantic Oscillation
 407 (NAO) exhibits higher EKE, due to an increase in baroclinic instability, thus suggest-
 408 ing more coherent eddies, we do not find a correlation between the $cEddy_n$ or the $\langle |cEddy_{amp}| \rangle$
 409 in the Gulf Stream and the NAO index. Similar to the signal observed in the hemispheric
 410 analysis, the eddy count seasonal cycle follows the wind maximum lagging by \sim 3 months,
 411 while the amplitude of the coherent eddies lags by \sim 6 months.

421 The variability of the $cEddy_n$ and $\langle |cEddy_{amp}| \rangle$ in the Kuroshio Current are weakly
 422 anti-correlated (-0.41; Figure 10). However, on average 56% of the energy in the region
 423 corresponds to CEKE. As observed in the Gulf Stream, there is an important seasonal
 424 cycle in the boundary current extension, where the eddy count seasonal cycle peak oc-
 425 curs in March, lagging the wind maximum by \sim 3 months (January). Meanwhile, the am-
 426 plitude of the coherent eddies lags the wind maximum by \sim 6 months (June).

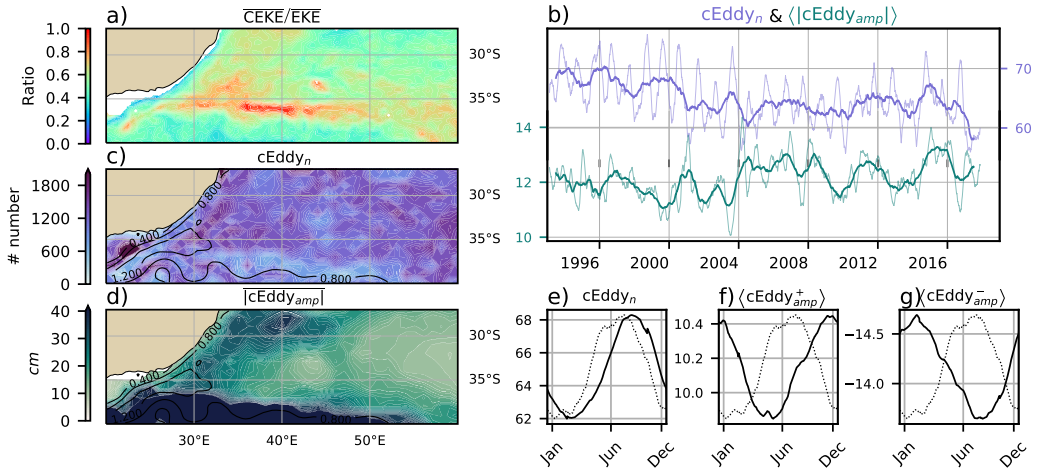
433 In the Southern Hemisphere the strongest boundary current, the Agulhas Current,
 434 shows similar behavior to its counterparts in the Northern Hemisphere (Figure 11). On
 435 average, coherent eddies in the Agulhas Current contain \sim 56% of the energy, meanwhile
 436 the $cEddy_n$ seasonal peak occurs in August, while the $\langle |cEddy_{amp}| \rangle$ peak occurs in January-
 437 February. The seasonal lag between the winds, eddy count, and eddy amplitude in each
 438 of the WBC extensions is interpreted as being analogous to the lagged response of co-
 439 herent eddy properties (Figure 6) due to eddy-eddy interactions, consistent with the in-
 440 verse cascade of energy.



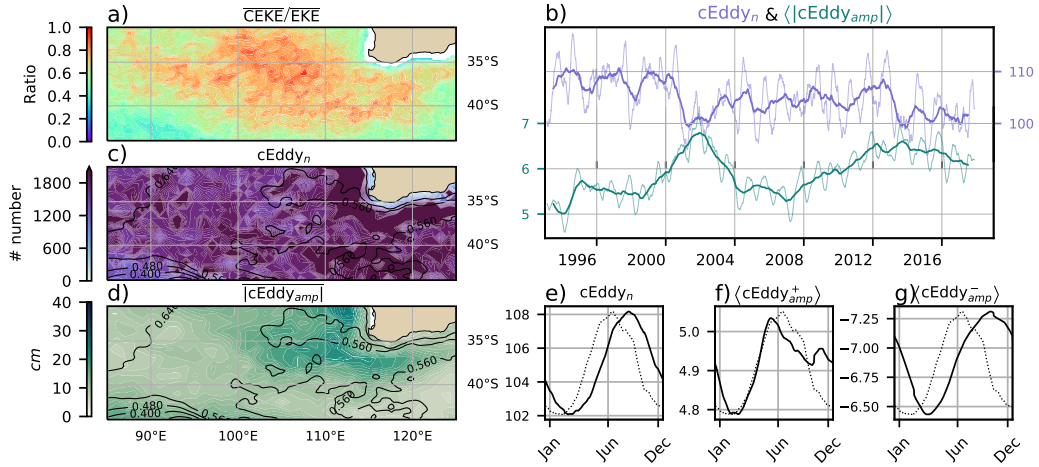
412 **Figure 9.** Climatology of the eddy field and coherent eddy field in the Gulf Stream. a) Ratio
 413 of mean coherent eddy kinetic energy ($\overline{\text{CEKE}}$) versus mean eddy kinetic energy ($\overline{\text{EKE}}$); b) Thick
 414 lines show the running average over 2 years and thin lines show the running average over 90 days
 415 of the coherent eddy number sum and the average coherent eddy amplitude; c) Map of the num-
 416 ber of eddies; d) Map of the average coherent eddy amplitude; e) Seasonal cycle of the number
 417 of eddies ($c\text{Eddy}_n$); f) Seasonal cycle of the positive coherent eddy amplitude ($\langle c\text{Eddy}_{amp}^+ \rangle$),
 418 and g) Seasonal cycle of the negative coherent eddy amplitude ($\langle c\text{Eddy}_{amp}^- \rangle$). Contours in maps
 419 correspond to mean sea surface height (m). Dotted lines show the seasonal cycle of the wind
 420 magnitude.



427 **Figure 10.** As in Figure 9, only showing the climatology of the eddy field and coherent eddy
 428 field in the Kuroshio extension. a) Ratio of mean coherent eddy kinetic energy ($\overline{\text{CEKE}}$) versus
 429 mean eddy kinetic energy ($\overline{\text{EKE}}$); b) Time-series of the coherent eddy number and the average
 430 coherent eddy amplitude; c) Map of the number of eddies; d) Map of the average coherent eddy
 431 amplitude; Seasonal cycle of the e) number of eddies; f) positive coherent eddy amplitude, and g)
 432 negative coherent eddy amplitude.



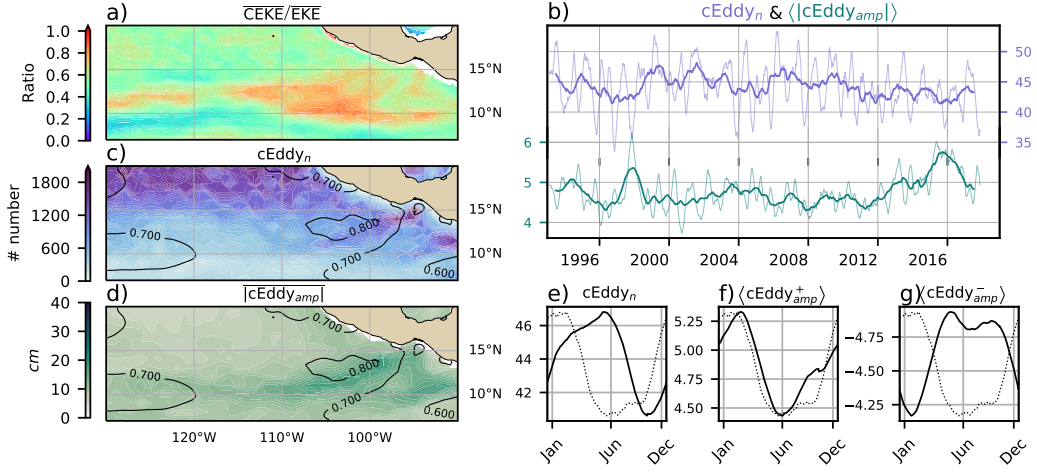
441 **Figure 11.** As in Figure 9, only showing the climatology of the eddy field and coherent eddy
 442 field in the Agulhas Current. a) Ratio of mean coherent eddy kinetic energy ($\overline{\text{CEKE}}$) versus
 443 mean eddy kinetic energy ($\overline{\text{EKE}}$); b) Time-series of the coherent eddy number and the average
 444 coherent eddy amplitude; c) Map of the number of eddies; d) Map of the average coherent eddy
 445 amplitude; Seasonal cycle of the e) number of eddies; f) positive coherent eddy amplitude, and g)
 446 negative coherent eddy amplitude.



457 **Figure 12.** As in Figure 9, only showing the climatology of the eddy field and coherent eddy
 458 field in the Leeuwin Current. a) Ratio of mean coherent eddy kinetic energy (\overline{CEKE}) versus
 459 mean eddy kinetic energy (\overline{EKE}); b) Time-series of the coherent eddy number and the average
 460 coherent eddy amplitude; c) Map of the number of eddies; d) Map of the average coherent eddy
 461 amplitude; Seasonal cycle of the e) number of eddies; f) positive coherent eddy amplitude, and g)
 462 negative coherent eddy amplitude.

447 Coherent eddies dominate the EKE field in other regions such as the Leeuwin Cur-
 448 rent (Figure 12), where 65% of the energy is contained in coherent eddies. The Leeuwin
 449 region is not characterized by having a large EKE, however, a considerable abundance
 450 of eddies and large eddy amplitudes are observed in the region. The time-series reveal
 451 a significant increase in the $\langle |cEddy_{amp}| \rangle$, while the $cEddy_n$ has decreased over the last
 452 3 decades. The seasonal cycle shows that the $cEddy_n$ peak occurs in August, 3 months
 453 after the maximum winds (June). Meanwhile, the $\langle cEddy_{amp}^+ \rangle$ responds in synchrony
 454 to the winds, and the $\langle cEddy_{amp}^- \rangle$ is in phase with the seasonal cycle of the eddy num-
 455 ber ($cEddy_n$). Hence, this region contrasts with the behavior of WBC extensions, and
 456 showcases the spatial variability of the seasonal cycle of coherent eddies.

463 Another region with important contributions to the coherent eddy field is the East
 464 Tropical Pacific (Tehuantepec region; Figure 13), where coherent eddies contain $\sim 58\%$
 465 of the energy. In fact, coherent eddy generation in this region is modulated by winds and
 466 coastally trapped waves which produce a strong horizontal and vertical shear (baroclinic
 467 and barotropic instabilities; Zamudio et al., 2006). Furthermore, the equatorial gener-



476 **Figure 13.** As in Figure 9, only showing the climatology of the eddy field and coherent eddy
 477 field in the East Tropical Pacific. a) Ratio of mean coherent eddy kinetic energy ($\overline{\text{CEKE}}$) versus
 478 mean eddy kinetic energy ($\overline{\text{EKE}}$); b) Time-series of the coherent eddy number and the average
 479 coherent eddy amplitude; c) Map of the number of eddies; d) Map of the average coherent eddy
 480 amplitude; Seasonal cycle of the e) number of eddies; f) positive coherent eddy amplitude, and g)
 481 negative coherent eddy amplitude.

468 ated waves propagating along the coast have an important interannual variability ob-
 469 servable in the $\langle |c\text{Eddy}_{amp}| \rangle$ time-series, where El Niño events are notable during 1997
 470 and 2015 (Figure 13b). The seasonal cycle of $c\text{Eddy}_n$, $\langle c\text{Eddy}_{amp}^+ \rangle$, and $\langle c\text{Eddy}_{amp}^- \rangle$ sup-
 471 port the idea of a coherent eddy response to two different coherent eddy generation mech-
 472 anisms; the number of eddies lags by ~ 3 months from the winds, while the $\langle c\text{Eddy}_{amp}^+ \rangle$
 473 is in phase with the winds and the time of maximum trapped wave activity (winter; Za-
 474 mudio et al., 2006), while the $\langle c\text{Eddy}_{amp}^- \rangle$ could be a consequence of eddy-eddy inter-
 475 actions.

482 7 Discussion and Conclusions

483 We have investigated the contribution of coherent eddies to the total kinetic en-
 484 ergy field using available satellite observations. We found that around half of the EKE
 485 is explained by coherent eddies. This half is concentrated in eddy-rich regions where a
 486 recent multi-decadal intensification of the eddy field has been observed (Martínez-Moreno
 487 et al., 2021). The energy contained by eddies is larger than the previous estimate of 40%

488 by Chelton et al. (2011). Although there are differences in the identification criteria of
 489 both eddy identification methods, the main cause of the difference is likely to be the life-
 490 span and amplitude filters. These filters are widely used to track individual eddies in space
 491 and time, however, interactions between eddies in energetic regions may obscure the abun-
 492 dance and influence of short-lived coherent eddies. Filters are not used in this study, and
 493 indeed a lack of filters could facilitate an over-estimation of the energy contained by
 494 coherent eddies, when mis-identifying or mis-fitting a coherent eddy.

495 It should also be noted that regions with first baroclinic Rossby radius of defor-
 496 mation smaller than 10km cannot be resolved by satellite observations. Thus, the en-
 497 ergy contained in coherent eddies around latitudes of 60° and those near the shore are
 498 missed from this estimate, and their role in the seasonal cycle and local dynamics remains
 499 unknown. New satellite altimeter missions (e.g. Surface Water and Ocean Topography;
 500 SWOT) may allow estimates of the energy contained in mesoscale coherent eddies out-
 501 side the subtropical regions and over the continental slope.

502 Hemisphere-wide variability indicates a strong seasonal cycle of the EKE, CEKE,
 503 and eddy properties. The seasonal cycle of the CEKE in each hemisphere occurs as a
 504 consequence of numerous small coherent eddies interacting with each other (eddy-eddy
 505 interactions) and resulting in stronger, larger and more energetic (but fewer) coherent
 506 eddies during summer, a few months after the yearly coherent eddy number maximum.
 507 This result reveals eddy-eddy interactions and thus the transfer of energy from smaller
 508 coherent eddies to larger coherent eddies could explain the observed seasonal cycle of CEKE
 509 and coherent eddies properties.

510 Coherent eddy properties reveal a non-uniform long-term readjustment of the mesoscale
 511 eddy field. Overall, the eddy number has decreased globally at a significant rate of \sim 35
 512 eddies per decade from \sim 4000 eddies identified globally on average each day. Despite the
 513 small changes in the total eddy numbers, large proportions of the ocean show a major
 514 strengthening of the mesoscale coherent eddy amplitude at rates greater than \sim 1 cm per
 515 decade. This strengthening of the coherent eddy amplitude is attributed to an intensi-
 516 fication of each coherent eddy polarity, rather than a readjustment of the coherent eddy
 517 field to sea level rise. In other words, the coherent eddy amplitude intensification is oc-
 518 ccurring in both coherent eddy polarities and a proportion of the previously observed read-
 519 justments in the eddy field to long-term changes in the ocean forcing (Hu et al., 2020;

520 Wunsch, 2020; Martínez-Moreno et al., 2021). This long-term readjustment reveals an
521 intensification of the coherent eddy field, possibly due to long-term readjustments in the
522 ocean baroclinic and barotropic instabilities, as well as the strength of the winds.

523 The reconstruction of the coherent eddies and their statistics has revealed regions
524 with important coherent eddy contributions and a distinct seasonal evolution of the co-
525 herent eddies. Western boundary current (WBC) extensions generate eddies through the
526 instability of the main currents and the seasonal cycle of coherent eddies, CEKE, and
527 thus EKE could be associated with an inverse energy cascade observable through lagged
528 seasonal cycles in the coherent eddy statistics. In addition, the amplitude of the seasonal
529 cycle in WBC extensions is two times larger than any other region, thus the seasonal-
530 ity of the coherent eddies in WBC extensions dominates the hemispheric seasonal cy-
531 cle. Furthermore, the seasonal lag of the inverse energy cascade is coupled with the pres-
532 ence of fronts (Qiu et al., 2014), such as the case for WBC extensions, and our results
533 are consistent with the notion of baroclinic instability generating eddies and, via eddy-
534 eddy interactions, a lagged inverse energy cascade.

535 The use of satellite observations in this study limits our ability to quantify the im-
536 portance of the inverse energy cascade seasonality in the control of the coherent eddy
537 seasonal cycle. As mentioned above, there is robust evidence of an increase in eddy-eddy
538 interactions, however we cannot discard important contributions from other processes
539 such as the seasonal cycle of forcing, stratification, and instabilities, which are crucial
540 in the generation of coherent eddies. Although this study can provide a descriptive re-
541 sponse of the coherent eddy field, further work is needed to assess the role of eddy-eddy
542 interactions in our changing climate, ocean dynamics, and biogeochemical processes. Fur-
543 thermore, the SWOT mission could allow us to advance our understanding of eddy-eddy
544 interactions and the seasonal cycle of scales smaller than mesoscale, which may provide
545 further evidence of the inverse energy cascade driving the coherent eddy seasonality. Cur-
546 rent generation climate models have just started to resolve mesoscale dynamics, thus,
547 the presented estimate of energy in coherent eddies from satellite observations could be
548 used as a benchmark that facilitates the evaluation of such models, and to quantify the
549 energy contained by mesoscale and more specifically coherent eddies in future climate
550 projections.

551 **Acknowledgments**

The Chelton & Schlax (2013) dataset was produced by SSALTO/DUACS and distributed by AVISO+ (<https://www.aviso.altimetry.fr/>) with support from CNES, developed and validated in collaboration with E.Mason at IMEDEA. Global coherent eddy reconstruction, coherent and non-coherent eddy kinetic energy datasets, in addition to gridded coherent eddy tracking datasets are publicly available at (<https://doi.org/10.5281/zenodo.4646429>). All analyses and figures in this manuscript are reproducible via Jupyter notebooks and instructions can be found in the Github repository `CEKE_climatology` (https://github.com/josuemtzmo/CEKE_climatology). Trends used the Python Package `xarrayMannKendall` (<https://doi.org/10.5281/zenodo.4458776>). J.M.-M. was supported by the Consejo Nacional de Ciencia y Tecnología (CONACYT), Mexico funding. M.H.E. is supported by the Centre for Southern Hemisphere Oceans Research (CSHOR), a joint research centre between Qingdao National Laboratory for Marine Science and Technology (QNL), Commonwealth Scientific and Industrial Research Organisation (CSIRO), University of New South Wales (UNSW), and the University of Tasmania (UTAS). Analyses were undertaken on the National Computational Infrastructure in Canberra, Australia, which is supported by the Australian Commonwealth Government.

568 **References**

- 569 Arbic, B. K., Polzin, K. L., Scott, R. B., Richman, J. G., & Shriver, J. F. (2013).
 570 On Eddy Viscosity, Energy Cascades, and the Horizontal Resolution of Gridded
 571 Satellite Altimeter Products*. *Journal of Physical Oceanography*, 43(2), 283–300.
 572 doi: 10.1175/jpo-d-11-0240.1
- 573 Ashkezari, M. D., Hill, C. N., Follett, C. N., Forget, G., & Follows, M. J. (2016).
 574 Oceanic eddy detection and lifetime forecast using machine learning methods.
 575 *Geophysical Research Letters*, 43(23). doi: 10.1002/2016gl071269
- 576 Beron-Vera, F. J., Wang, Y., Olascoaga, M. J., Goni, G. J., & Haller, G. (2013). Ob-
 577 jective Detection of Oceanic Eddies and the Agulhas Leakage. *Journal of Physical
 578 Oceanography*, 43(7), 1426–1438. doi: 10.1175/JPO-D-12-0171.1
- 579 Bouali, M., Sato, O. T., & Polito, P. S. (2017). Temporal trends in sea surface tem-
 580 perature gradients in the South Atlantic Ocean. *Remote Sensing of Environment*,
 581 194, 100–114. doi: 10.1016/j.rse.2017.03.008
- 582 Callies, J., Flierl, G., Ferrari, R., & Fox-Kemper, B. (2015). The role of mixed-layer

- 583 instabilities in submesoscale turbulence. *Journal of Fluid Mechanics*, 788, 5–41.
- 584 doi: 10.1017/jfm.2015.700
- 585 Cane, M. A., Clement, A. C., Kaplan, A., Kushnir, Y., Pozdnyakov, D., Seager, R.,
 586 ... Murtugudde, R. (1997). Twentieth-Century Sea Surface Temperature Trends.
 587 *Science*, 275(5302), 957–960. doi: 10.1126/science.275.5302.957
- 588 Chaudhuri, A. H., Gangopadhyay, A., & Bisagni, J. J. (2009). Interannual variabil-
 589 ity of Gulf Stream warm-core rings in response to the North Atlantic Oscillation.
 590 *Continental Shelf Research*, 29(7), 856–869. doi: 10.1016/j.csr.2009.01.008
- 591 Chelton, D. B., A. d. R., Schlax, M. G., Naggar, K., & Siwertz, N. (1998). Geo-
 592 graphical variability of the first baroclinic Rossby radius of deformation. *Journal*
 593 *of Physical Oceanography*, 28(3), 433–460. doi: 10.1175/1520-0485(1998)028<433:
 594 GVOTFB>2.0.CO;2
- 595 Chelton, D. B., Gaube, P., Schlax, M. G., Early, J. J., & Samelson, R. M. (2011).
 596 The influence of nonlinear mesoscale eddies on near-surface oceanic chlorophyll.
 597 *Science*, 334(6054), 328–32. doi: 10.1126/science.1208897
- 598 Chelton, D. B., & Schlax, M. G. (2013). *Mesoscale eddies in altimeter observations*
 599 *of ssh*.
- 600 Chelton, D. B., Schlax, M. G., Samelson, R. M., & de Szoeke, R. A. (2007). Global
 601 observations of large oceanic eddies. *Geophysical Research Letters*, 34(15),
 602 L15606. doi: 10.1029/2007GL030812
- 603 CMEMS. (2017). The Ssalto/Duacs altimeter products were produced and dis-
 604 tributed by the Copernicus Marine and Environment Monitoring Service. *Aviso*
 605 *Dataset*. Retrieved from <https://www.aviso.altimetry.fr/>
- 606 Cui, W., Wang, W., Zhang, J., & Yang, J. (2020). Identification and census statis-
 607 tics of multicore eddies based on sea surface height data in global oceans. *Acta*
 608 *Oceanologica Sinica*, 39(1), 41–51. doi: 10.1007/s13131-019-1519-y
- 609 Faghmous, J. H., Frenger, I., Yao, Y., Warmka, R., Lindell, A., & Kumar, V. (2015,
 610 6). A daily global mesoscale ocean eddy dataset from satellite altimetry. *Scientific*
 611 *Data*, 2, 150028 EP -. doi: 10.1038/sdata.2015.28
- 612 Ferrari, R., & Wunsch, C. (2009). Ocean Circulation Kinetic Energy: Reservoirs,
 613 Sources, and Sinks. *Annual Review of Fluid Mechanics*, 41(1), 253–282. doi: 10
 614 .1146/annurev.fluid.40.111406.102139
- 615 Frenger, I., Gruber, N., Knutti, R., & Münnich, M. (2013). Imprint of Southern

- 616 Ocean eddies on winds, clouds and rainfall. *Nature Geoscience*, 6(8), 608 EP -.
617 doi: 10.1038/ngeo1863
- 618 Frenger, I., Münnich, M., Gruber, N., & Knutti, R. (2015). Southern Ocean eddy
619 phenomenology. *Journal of Geophysical Research: Oceans*, 120(11), 7413-7449.
620 doi: 10.1002/2015JC011047
- 621 Fu, L., Chelton, D., Le Traon, P., & Oceanography, M. R. (2010). Eddy dynamics
622 from satellite altimetry. *Oceanography*, 23(4), 14-25. doi: 10.2307/24860859
- 623 Gill, A., Green, J., & Simmons, A. (1974). Energy partition in the large-scale ocean
624 circulation and the production of mid-ocean eddies. *Deep Sea Res Oceanogr Abstr*,
625 21(7), 499-528. doi: 10.1016/0011-7471(74)90010-2
- 626 Hogg, A. M., & Blundell, J. R. (2006). Interdecadal variability of the southern
627 ocean. *Journal of Physical Oceanography*, 36(8), 1626-1645. doi: 10.1175/
628 JPO2934.1
- 629 Hogg, A. M., Meredith, M. P., Chambers, D. P., Abrahamsen, E. P., Hughes,
630 C. W., & Morrison, A. K. (2015). Recent trends in the Southern Ocean
631 eddy field. *Journal of Geophysical Research: Oceans*, 120(1), 257-267. doi:
632 10.1002/2014JC010470
- 633 Hu, S., Sprintall, J., Guan, C., McPhaden, M. J., Wang, F., Hu, D., & Cai,
634 W. (2020, 2). Deep-reaching acceleration of global mean ocean circula-
635 tion over the past two decades. *Science Advances*, 6(6), eaax7727. doi:
636 10.1126/sciadv.aax7727
- 637 Japan Meteorological Agency, Japan. (2013). *Jra-55: Japanese 55-year reanalysis*,
638 *daily 3-hourly and 6-hourly data*. Boulder CO: Research Data Archive at the Na-
639 tional Center for Atmospheric Research, Computational and Information Systems
640 Laboratory. Retrieved from <https://doi.org/10.5065/D6HH6H41>
- 641 Kang, D., & Curchitser, E. N. (2013). Gulf stream eddy characteristics in a high-
642 resolution ocean model. *Journal of Geophysical Research: Oceans*, 118(9), 4474-
643 4487. Retrieved from <https://agupubs.onlinelibrary.wiley.com/doi/abs/10.1002/jgrc.20318> doi: <https://doi.org/10.1002/jgrc.20318>
- 644 Kang, D., & Curchitser, E. N. (2017). On the Evaluation of Seasonal Variability of
645 the Ocean Kinetic Energy. *Geophysical Research Letters*, 47, 1675-1583. doi: 10
646 .1175/JPO-D-17-0063.1
- 647 Li, G., Cheng, L., Zhu, J., Trenberth, K. E., Mann, M. E., & Abraham, J. P. (2020).

- 649 Increasing ocean stratification over the past half-century. *Nature Climate Change*,
650 1–8. doi: 10.1038/s41558-020-00918-2
- 651 Martínez-Moreno, J., Hogg, A. M., England, M., Constantinou, N. C., Kiss, A. E.,
652 & Morrison, A. K. (2021). Global changes in oceanic mesoscale currents over the
653 satellite altimetry record. *Journal of Advances in Modeling Earth Systems*, 0(ja).
654 doi: 10.1029/2019MS001769
- 655 Martínez-Moreno, J., Hogg, A. M., Kiss, A. E., Constantinou, N. C., & Morrison,
656 A. K. (2019). Kinetic energy of eddy-like features from sea surface altime-
657 try. *Journal of Advances in Modeling Earth Systems*, 11(10), 3090–3105. doi:
658 10.1029/2019MS001769
- 659 Patel, R. S., Llort, J., Strutton, P. G., Phillips, H. E., Moreau, S., Pardo, P. C.,
660 & Lenton, A. (2020). The Biogeochemical Structure of Southern Ocean
661 Mesoscale Eddies. *Journal of Geophysical Research: Oceans*, 125(8). doi:
662 10.1029/2020jc016115
- 663 Pilo, G. S., Mata, M. M., & Azevedo, J. L. L. (2015). Eddy surface properties and
664 propagation at Southern Hemisphere western boundary current systems. *Ocean
665 Science*, 11(4), 629–641. doi: 10.5194/os-11-629-2015
- 666 Qiu, B. (1999). Seasonal Eddy Field Modulation of the North Pacific Subtropical
667 Countercurrent: TOPEX/Poseidon Observations and Theory. *Journal of Physical
668 Oceanography*, 29(10), 2471–2486. doi: 10.1175/1520-0485(1999)029<2471:sefmot>2
669 .0.co;2
- 670 Qiu, B., & Chen, S. (2004). Seasonal Modulations in the Eddy Field of the South
671 Pacific Ocean. *Journal of Physical Oceanography*, 34(7), 1515–1527. doi: 10.1175/
672 1520-0485(2004)034<1515:smitef>2.0.co;2
- 673 Qiu, B., Chen, S., Klein, P., Sasaki, H., & Sasai, Y. (2014). Seasonal Mesoscale
674 and Submesoscale Eddy Variability along the North Pacific Subtropical Coun-
675 tercurrent. *Journal of Physical Oceanography*, 44(12), 3079–3098. doi:
676 10.1175/JPO-D-14-0071.1
- 677 Ruela, R., Sousa, M. C., deCastro, M., & Dias, J. M. (2020). Global and regional
678 evolution of sea surface temperature under climate change. *Global and Planetary
679 Change*, 190, 103190. doi: 10.1016/j.gloplacha.2020.103190
- 680 Sasaki, H., Klein, P., Qiu, B., & Sasai, Y. (2014). Impact of oceanic-scale inter-
681 actions on the seasonal modulation of ocean dynamics by the atmosphere. *Nature*

- 682 *Communications*, 5(1), 5636. doi: 10.1038/ncomms6636
- 683 Schubert, R., Schwarzkopf, F. U., Baschek, B., & Biastoch, A. (2019). Submesoscale
684 Impacts on Mesoscale Agulhas Dynamics. *Journal of Advances in Modeling Earth
685 Systems*, 11(8), 2745–2767. doi: 10.1029/2019ms001724
- 686 Siegel, D., Peterson, P., DJ, M., Maritorena, S., & Nelson, N. (2011). Bio-optical
687 footprints created by mesoscale eddies in the Sargasso Sea. *Geophysical Research
688 Letters*, 38(13), n/a-n/a. doi: 10.1029/2011GL047660
- 689 Uchida, T., Abernathey, R., & Smith, S. (2017). Seasonality of eddy kinetic energy
690 in an eddy permitting global climate model. *Ocean Modelling*, 118, 41-58. doi: 10
691 .1016/j.ocemod.2017.08.006
- 692 Wunsch, C. (2020). Is The Ocean Speeding Up? Ocean Surface Energy Trends.
693 *Journal of Physical Oceanography*, 50(11), 1–45. doi: 10.1175/jpo-d-20-0082.1
- 694 Wunsch, C., & Ferrari, R. (2004). Vertical mixing, energy, and the general circulation
695 of the oceans. *Annual Review of Fluid Mechanics*, 36(1), 281–314. doi: 10
696 .1146/annurev.fluid.36.050802.122121
- 697 Wyrtki, K., Magaard, L., & Hager, J. (1976). Eddy energy in the oceans. *Journal of
698 Geophysical Research*, 81(15), 2641-2646. doi: 10.1029/JC081i015p02641
- 699 Yue, S., & Wang, C. (2004). The Mann-Kendall Test Modified by Effective Sample
700 Size to Detect Trend in Serially Correlated Hydrological Series. *Water Resources
701 Management*, 18(3), 201–218. doi: 10.1023/b:warm.0000043140.61082.60
- 702 Zamudio, L., Hurlbert, H. E., Metzger, E. J., Morey, S. L., O'Brien, J. J., Tilburg,
703 C., & Zavala-Hidalgo, J. (2006). Interannual variability of Tehuantepec ed-
704 dies. *Journal of Geophysical Research: Oceans (1978–2012)*, 111(C5). doi:
705 10.1029/2005JC003182